Available online at www.sciencedirect.com
ScienceDirect
Geochimica et Cosmochimica Acta 71 (2007) 481–496
Geochimica
www.elsevier.com/locate/gca

Extension of lattice strain theory to mineral/mineral rare-earth element partitioning: An approach for assessing disequilibrium and developing internally consistent partition coefficients between olivine, orthopyroxene, clinopyroxene and basaltic melt

Cin-Ty Aeolus Lee [a,*], Artemis Harbert [a], William P. Leeman [b]

[a] *Department of Earth Science, MS-126, Rice University, 6100 Main Street, Houston, TX 77005, USA*
[b] *Earth Sciences Division, National Science Foundation, 4201 Wilson Blvd., Arlington, VA 2230, USA*

Received 6 March 2006; accepted in revised form 20 September 2006

Abstract

Olivine/melt and orthopyroxene/melt rare-earth element (REE) partition coefficients consistent with clinopyroxene/melt partition coefficients were determined indirectly from subsolidus partitioning between olivine, orthopyroxene, and clinopyroxene after suitable correction for temperature. Heavy- and middle-REE ratios for olivine/clinopyroxene and orthopyroxene/clinopyroxene pairs correlate negatively with effective cationic radius, whereas those for the light REEs correlate positively with cationic radius, generating a U-shaped pattern in apparent mineral/clinopyroxene partition coefficients versus cationic radius. Lattice strain models of partitioning modified for subsolidus conditions yield negative correlations of olivine/clinopyroxene and orthopyroxene/clinopyroxene with respect to cationic radii, predicting well the measured partitioning behaviors of the heavy and middle REEs but not that of the light REEs. The light-REE systematics cannot be explained with lattice strain theory and, instead, can be explained by disequilibrium enrichment of the light REEs in melt inclusions or on the rims of olivine and orthopyroxene. Realistic light-REE partition coefficients were thus extrapolated from the measured heavy- and middle-REE partition coefficients using the lattice strain model. Light REE olivine/melt and orthopyroxene/melt partition coefficients calculated in this manner are lower than most published values, but agree reasonably well with partitioning experiments using the most recent in situ analytical techniques (secondary-ionization mass spectrometry and laser ablation inductively coupled plasma mass spectrometry). These new olivine/melt and orthopyroxene/melt partition coefficients are useful for accurate modeling of the REE contents of clinopyroxene-poor to -free lithologies, such as harzburgitic residues of melting. Finally, the application of the lattice strain theory to subsolidus conditions represents a framework for assessing the degree of REE disequilibrium in a rock.

1. Introduction

The upper mantle is dominated by peridotite, which is composed of clinopyroxene, orthopyroxene, olivine and an aluminous phase, such as garnet, spinel or plagioclase depending on pressure. Clinopyroxene has by far the strongest affinity for incompatible trace elements so that clinopyroxene, when present, controls the distribution of incompatible trace elements during melting. There are, however, some processes where clinopyroxene is absent or scarce, such as harzburgite melting (e.g., melting of recycled oceanic lithospheric mantle in plumes or melting of subcontinental lithospheric mantle during extension). In these cases, olivine and orthopyroxene control trace-element partitioning. This paper addresses mineral/melt partition coefficients for rare-earth elements (REEs) in olivine and orthopyroxene to better understand how these elements are distributed during the partial melting of harzburgitic lithologies.

Our understanding of trace-element partitioning between olivine, orthopyroxene and melt is clouded by large

* Corresponding author. Fax: +1 713 348 5214.
E-mail addresses: ctlee@rice.edu (C.-T. A. Lee), WLeeman@nsf.gov (W.P. Leeman).

0016-7037/$ - see front matter © 2006 Elsevier Inc. All rights reserved.
doi:10.1016/j.gca.2006.09.014

variations in values presented in the literature (Fig. 1). Tabulated REE partition coefficients (Fig. 1) vary by one order of magnitude in orthopyroxene and by four orders of magnitude in olivine (Onuma et al., 1968; Schnetzler and Philpotts, 1970; Matsui et al., 1977; McKay and Weill, 1977; Larsen, 1979; Shimizu et al., 1982; Fujimaki et al., 1984; Irving and Frey, 1984; McKay, 1986; McKenzie and O'Nions, 1991; Nielsen et al., 1992; Hauri et al., 1993; Kennedy et al., 1993; Schwandt and McKay, 1998; McDade et al., 2003). In contrast, REE partitioning in clinopyroxene is much better understood (Hart and Dunn, 1993; Blundy and Wood, 1994; Hauri et al., 1994; Wood and Blundy, 1997, 2001, 2003). This disparity is related to the much higher concentrations of REEs in clinopyroxenes than in olivine and orthopyroxene (Stosch, 1982; Kennedy et al., 1993; Eggins et al., 1998; Witt-Eickschen and O'Neill, 2005). As a consequence, determination of olivine and orthopyroxene REE partition coefficients from natural phenocryst-magma pairs or experiments is problematic owing to insufficient analytical sensitivity, contamination of grain boundaries by REE-enriched glasses or accessory phases, and contamination of grain interiors by microscopic melt or fluid inclusions. Finally, the slow diffusivities of the REEs compared to the major divalent cations making up these minerals often results in disequilibrium concentrations (Van Orman et al., 2001).

Here, we combine empirical observation and theory to develop mineral/melt REE-partition coefficients for olivine and orthopyroxene, which are internally consistent with the better understood partitioning of clinopyroxene. We adopt an indirect approach based initially on the measurement of apparent subsolidus mineral/mineral partition coefficients in peridotite xenoliths followed by suitable correction for temperature and bootstrapping with known

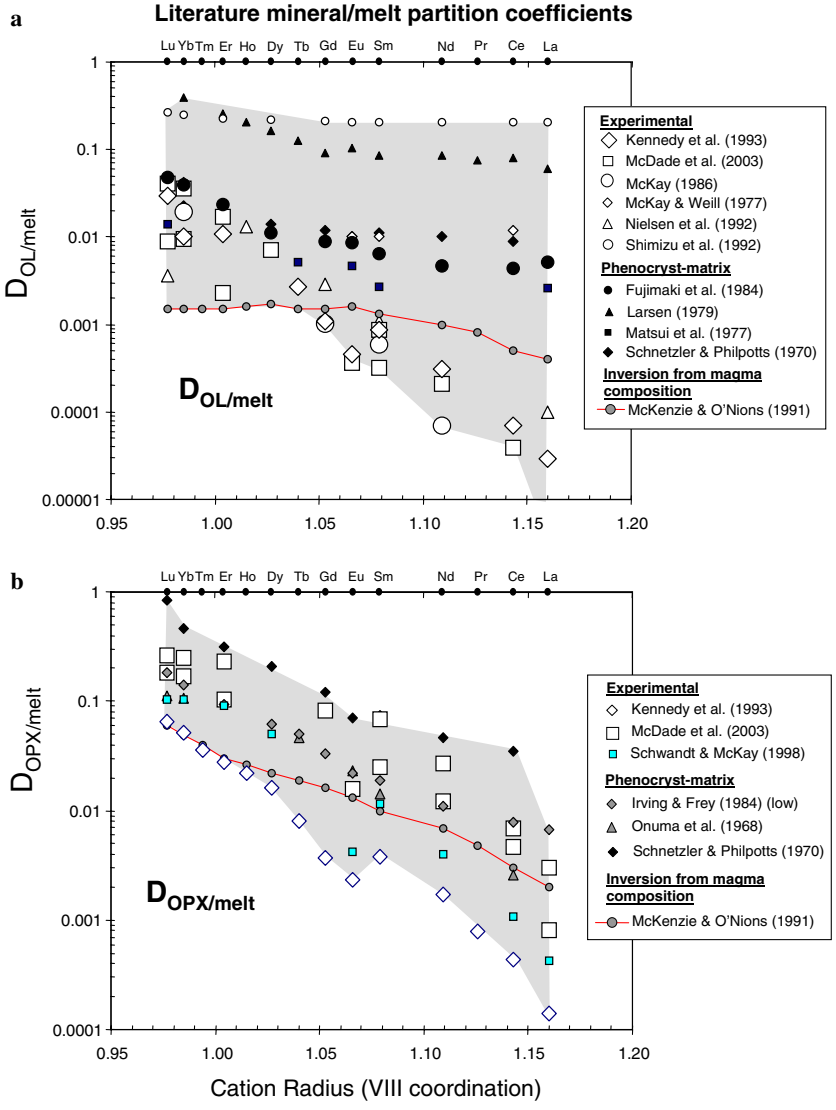

Fig. 1. Ol/melt (a) and Opx/melt (b) partition coefficients based on a literature compilation and plotted against cationic radii in 8-fold coordination. References are given in the legend and text, and are categorized into measurements based on phenocryst-magma pairs, experiments, and inversions of magma compositions.

clinopyroxene/melt partition coefficients (Stosch, 1982). The advantages of this approach are that (1) all three mineral phases are present, (2) these minerals have resided in the mantle for millions of years at high temperature, presumably ensuring equilibrium, and (3) the minerals are large enough to be picked and dissolved for accurate measurement of trace elements in very low concentrations. However, a potential complication is that, despite the long residence in the mantle, xenoliths often suffer from recent contamination by metasomatic fluids or the host lava itself, raising the issue of whether trace element equilibrium between minerals has been compromised. Our data are thus examined in the context of a physical model based on elastic strain theory modified for subsolidus mineral/mineral partitioning. We show that elastic strain theory predicts well the mineral/mineral distribution of heavy to middle REEs (HREE and MREE), but does not in itself account for the distribution of the light REEs (LREEs). The LREE systematics are best explained by disequilibrium effects associated with recent contamination on mineral surfaces or by fluid inclusions introduced from the host magma or its pre-eruptive precursor.

In summary, verification that lattice strain theory successfully predicts equilibrium mineral/mineral partitioning allows us to develop a new tool for ''seeing through'' or assessing the effects of disequilibrium. From extrapolation of the lattice strain theory, we are able to determine the true mineral/mineral partition coefficients for LREEs unadulterated by recent contamination or metasomatism. Conversion to mineral/melt partition coefficients then only requires a temperature correction and multiplication by a suitable clinopyroxene/melt partition coefficient. The end-result of our study is very similar to that of Witt-Eickschen and O'Neill (2005), but our approach differs fundamentally. These authors presented a purely empirical fit of their apparent partition coefficient data to cationic radii, whereas we present a physically meaningful model for explaining partitioning behavior. The agreement between these studies provides confidence that mineral/melt and mineral/mineral partitioning can be predicted by simple physical laws.

2. Methods

Three peridotite xenoliths were investigated. These are SC99-1 from San Carlos (Arizona), KH77-9 from Kilbourne Hole (New Mexico), and 68SAL21 from Salt Lake Crater on Oahu Island (Hawaii). All samples appeared fresh, showing no evidence for serpentinization or obvious infiltration of the host lava. Fresh and inclusion-free olivine, orthopyroxene and clinopyroxene grains were separated out. Mineral grains were not subjected to any cleaning or leaching treatments. Two to three grains were then combined (total weight of ~0.001 g) and weighed to the fifth-decimal on a Mettler–Toledo balance (a static blower was used on each sample prior to weighing). Each sample was dissolved in 0.5 mL of a 1:1 (by volume) mixture of concentrated HF–$HClO_4$ in a screw-top Teflon beaker at 115 °C for 24 h. This was followed by a complete open-air dry-down at 175 °C. This procedure was repeated once. The samples were then taken up in 2% (by weight) of HNO_3 for direct analysis by ICP-MS. A pure In solution was added to the final diluted solution to attain a final concentration of 1 ppb (by weight); the In signal was used to correct for instrumental drift.

Analyses of major and trace-elements were done by introducing solutions into a magnetic sector inductively coupled plasma mass spectrometer (ThermoFinnigan Element 2 ICP-MS). Major elements were analyzed using a mass resolution ($m/\Delta m$) of ~3000, while most trace elements were determined at a lower mass resolution of (300). Sample intensities were calibrated against three external basalt standards from the United States Geological Survey (two independently prepared BHVO-1 solutions and one BIR-1; (Eggins et al., 1997)) prepared in the same way as the sample. A peridotite standard (JP-1 or DTS-1) was used to calibrate Mg and Ni contents. Procedural blanks were also run. Analyses of Kilbourne Hole and Salt Lake Crater samples were done by Harbert. San Carlos samples were analyzed independently by Lee and Harbert.

The only major element not determined by ICP-MS was Si due to volatile loss of SiF_4 during dissolution. However, assuming that the total volatile content in the unaltered olivines, orthopyroxenes, and clinopyroxenes is negligible, the SiO_2 content was estimated by subtracting the total of all major element oxides from 100 wt% (Table 1). Recalculations of cation mole percents on 4 and 6 oxygen bases (olivine and pyroxene, respectively) are shown in Table 1.

3. Results

Mineral compositions are shown in Table 1. Mineral major element chemistries are within the range seen in minerals from peridotitic lithologies having whole-rock Mg#s (molar Mg/(Mg + Fe)) between 0.88 and 0.93 and are thus representative of peridotites believed to be melting residues (Lee, 2003). Equigranular textures and well-developed triple junctions suggest textural equilibrium. All samples are spinel peridotites and hence record last equilibration pressures less than 2 GPa. Equilibration temperatures calculated using two-pyroxene thermometry (Wells, 1977; Brey and Kohler, 1990) fell between 1000 and 1100 °C (a pressure of 1.5 GPa was assumed, but using 1 or 2 GPa does not change the result to within error of our major-element determinations by ICP-MS).

REE concentrations in olivine and orthopyroxene were divided by those in clinopyroxene to produce apparent ol/cpx, opx/cpx, and ol/opx partition coefficients (Table 2). These are plotted in Fig. 2 as a function of effective cationic radii (Onuma et al., 1968) assuming all REEs are in eightfold coordination (Shannon, 1976). Although it would be more realistic to consider sixfold coordinated radii for olivine, the use of the same set of effective radii for olivines and pyroxenes greatly simplifies the mathematical treat-

Table 1
Mineral chemistries (ICP-MS measurements)

	San Carlos (SC99-1)						Salt Lake Crater, Hawaii (68SAL21)						Killbourne Hole (KH77-9)					
	Ol		Opx		Cpx		Ol		Opx		Cpx		Ol		Opx		Cpx	
	ave $n=6$	1σ	ave $n=6$	1σ	ave $n=7$	1σ	ave $n=4$	1σ	ave $n=4$	1σ	ave $n=4$	1σ	ave $n=4$	1σ	ave $n=4$	1σ	ave $n=4$	1σ
Low mass resolution ICP-MS																		
	ppm		ppm		ppm		ppm		ppm		ppm		ppm		ppm		ppm	
La	0.0434	0.012	0.0484	0.0072	1.37	0.42	0.0550	0.0060	0.2595	0.04440	5.57	0.23	0.01810	0.0055	0.0189	0.0052	1.29	0.05
Ce	0.0606	0.007	0.0769	0.0129	4.08	0.90	0.0870	0.0134	0.4953	0.0618	18.0	0.3	0.0290	0.0068	0.0396	0.0070	4.74	0.07
Pr	0.0076	0.003	0.0118	0.0019	0.651	0.096	0.0107	0.0017	0.0592	0.0064	2.81	0.12	0.0036	0.0007	0.0072	0.0008	0.907	0.022
Nd	0.0235	0.009	0.0529	0.0087	3.61	0.24	0.0412	0.0080	0.2705	0.0257	14.2	0.5	0.0147	0.0021	0.0475	0.0035	5.58	0.07
Sm	0.0022	0.0006	0.0219	0.023	1.36	0.07	0.0082	0.0020	0.0781	0.061	3.74	0.12	0.0037	0.0006	0.0299	0.0007	2.15	0.03
Eu	0.0013	0.0005	0.0122	0.0017	0.549	0.031	0.0029	0.00068	0.031	0.002	1.29	0.03	0.0014	0.0002	0.0155	0.0004	0.853	0.012
Gd	0.0036	0.0013	0.0395	0.0028	1.44	0.12	0.0081	0.0018	0.1015	0.0057	3.70	0.10	0.0051	0.0009	0.0734	0.0012	2.98	0.05
Tb	0.0007	0.0001	0.0103	0.0004	0.295	0.017	0.0012	0.0003	0.0189	0.0008	0.0560	0.014	0.0010	0.0002	0.0174	0.0004	0.533	0.008
Dy	0.0055	0.0006	0.113	0.0047	2.32	0.14	0.0071	0.0012	0.1338	0.0048	3.05	0.05	0.0083	0.0012	0.160	0.003	3.50	0.07
Ho	0.0022	0.0004	0.0490	0.0005	0.726	0.010	0.0016	0.0003	0.0328	0.0006	0.556	0.005	0.0026	0.0003	0.0478	0.0009	0.772	0.016
Er	0.0108	0.0013	0.199	0.0035	2.18	0.02	0.0054	0.0005	0.1115	0.0025	1.44	0.02	0.0110	0.0011	0.184	0.003	2.17	0.04
Tm	0.0025	0.0002	0.0394	0.0012	0.319	0.013	0.0014	0.0001	0.0243	0.0005	0.237	0.002	0.0031	0.0002	0.0423	0.0009	0.366	0.007
Yb	0.0193	0.0012	0.246	0.015	1.60	0.14	0.0099	0.0004	0.1453	0.0042	1.16	0.02	0.0227	0.0012	0.259	0.004	1.75	0.04
Lu	0.0050	0.0002	0.0494	0.0009	0.255	0.009	0.0023	0.0000	0.0259	0.0007	0.161	0.003	0.0053	0.0003	0.0468	0.0009	0.246	0.005
Medium mass resolution ICP-MS	wt%		wt%		wt%		wt%		wt%		wt%		wt%		wt%		wt%	
Na_2O	0.0108	0.0016	0.126	0.0032	1.59	0.043	0.0131	0.002	0.232	0.038	2.89	0.11	0.0102	0.0002	0.132	0.0021	1.79	0.093
MgO	43.6	5.9	29.4	1.8	14.4	0.84	41.9	0.86	29.5	0.18	13.2	0.91	42.57	3.7	28.64	1.9	13.7	1.3
Al_2O_3	0.075	0.012	4.75	0.17	6.6	0.27	0.0379	0.008	4.45	0.045	6.046	0.15	0.0501	0.013	4.90	0.16	6.79	0.33
CaO	0.104	0.011	0.918	0.061	19.2	0.66	0.051	0.004	0.774	0.013	18.8	0.86	0.112	0.0133	0.859	0.040	19.5	1.21
MnO	0.144	0.0016	0.133	0.0054	0.0878	0.005	0.1532	0.002	0.1488	0.004	0.0937	0.004	0.141	0.009	0.136	0.008	0.0865	0.006
FeO	10.5	0.23	5.88	0.32	2.81	0.20	10.9	0.21	6.94	0.186	3.46	0.063	9.93	1.0	6.13	0.38	3.00	0.23
SiO_2 (by difference)	46		59		55		47		58		56		#47		59		55	
Mineral formula from ICP-MS	4 Oxygen		6 Oxygen		6 Oxygen		4 Oxygen		6 Oxygen		6 Oxygen		4 Oxygen		6 Oxygen		6 Oxygen	
Na	0.001		0.008		0.11		0.001		0.02		0.20		0.0010		0.009		0.12	
Mg	1.57		1.49		0.77		1.51		1.51		0.70		1.52		1.46		0.73	
Al	0.002		0.191		0.275		0.001		0.180		0.255		0.001		0.197		0.286	
Ca	0.003		0.034		0.733		0.001		0.028		0.722		0.003		0.031		0.747	
Mn	0.003		0.004		0.003		0.003		0.004		0.003		0.003		0.004		0.003	
Fe	0.21		0.17		0.08		0.22		0.20		0.10		0.210		0.17		0.09	
Si	1.10		2.01		1.97		1.13		1.99		1.99		1.13		2.02		1.97	
Sum	2.9		3.9		3.9		2.9		3.9		4.0		2.9		3.9		3.9	

Table 2
Apparent subsolidus partition coefficients (ppm/ppm)

		SC99-1				68SAL21				KH7-9			
	VIII cation radius (A°)	$D^{Ol/Cpx}$	1σ	$D^{Opx/Cpx}$	1σ	$D^{Ol/Cpx}$	1σ	$D^{Opx/Cpx}$	1σ	$D^{Ol/Cpx}$	1σ	$D^{Opx/Cpx}$	1σ
La	1.16	0.032	0.013	0.035	0.012	0.010	0.001	0.047	0.008	0.014	0.004	0.015	0.004
Ce	1.143	0.015	0.004	0.019	0.005	0.0048	0.0007	0.027	0.003	0.0061	0.0014	0.0084	0.0015
Pr	1.126	0.012	0.005	0.018	0.004	0.0038	0.0006	0.021	0.002	0.0040	0.0007	0.0080	0.0009
Nd	1.109	0.0065	0.0026	0.015	0.003	0.0029	0.0006	0.019	0.002	0.0026	0.0004	0.0085	0.0006
Sm	1.079	0.0016	0.0004	0.016	0.002	0.0022	0.0005	0.021	0.002	0.0017	0.0003	0.0139	0.0004
Eu	1.066	0.0023	0.0009	0.022	0.003	0.02	0.0005	0.024	0.002	0.0016	0.0003	0.018	0.001
Gd	1.053	0.0025	0.0009	0.027	0.003	0.02	0.0005	0.027	0.002	0.0017	0.0003	0.025	0.001
Tb	1.04	0.0022	0.0004	0.035	0.003	0.0022	0.0005	0.034	0.002	0.0019	0.033	0.033	0.001
Dy	1.027	0.0024	0.0003	0.049	0.004	0.0023	0.0004	0.0044	0.002	0.0024	0.0003	0.046	0.001
Ho	1.015	0.0031	0.0006	0.068	0.001	0.0028	0.0005	0.059	0.001	0.0033	0.0003	0.062	0.002
Er	1.004	0.0050	0.0006	0.091	0.002	0.0038	0.0004	0.077	0.002	0.0051	0.0005	0.085	0.002
Tm	0.994	0.0079	0.0006	0.124	0.0006	0.0057	0.0005	0.103	0.002	0.0083	0.0006	0.116	0.003
Yb	0.985	0.012	0.001	0.153	0.016	0.0085	0.004	0.125	0.004	0.013	0.001	0.148	0.004
Lu	0.977	0.020	0.001	0.194	0.008	0.014	0.000	0.161	0.005	0.022	0.001	0.190	0.005

1σ = 1 standard deviation.

ment of the partitioning model that we discuss later. We find that apparent ol/cpx, opx/cpx and ol/opx partition coefficients for the HREEs and MREEs (small cationic radius) correlate negatively with cationic radii while apparent LREE partition coefficients correlate positively with cationic radius. This results in an upward concave parabola or a "U-shaped" appearance on a plot of apparent partition coefficient versus cationic radius (Fig. 2). The shapes of these curves vary between samples as can be seen from the tendency of the curves to diverge or scatter in the LREE region. However, despite the scatter in the LREEs, the curves all collapse to roughly the same trend in the region of small cationic radii, which corresponds to the HREEs and MREEs.

We can also compare the results of our unleached mineral separates to the results of acid-leached bulk mineral dissolution studies of Stosch (1982) and Eggins et al. (1998). Apparent partition coefficients from these leaching studies plotted against cationic radius exhibit less extreme parabolic shapes compared to our data (Fig. 2). For example, opx/cpx partition coefficients decrease monotonically with increasing cationic radius. Ol/cpx curves appear to have "straightened out" slightly as can be seen by the displacement of the parabola minimum towards larger cationic radii compared to our unleached curves. What the leaching studies have in common with our results is that the partition coefficients of the HREEs and MREEs all collapse to the same trends seen in our data.

As a final comparison, we have also plotted apparent ol/cpx, opx/cpx and ol/opx partition coefficients from the peridotite melting experiments of McDade et al. (2003) run at 1.5 GPa and 1315 °C (e.g., above solidus temperatures). Unlike the bulk mineral dissolution approach taken by our study, the apparent partition coefficients reported in this study are based on in situ ion-microprobe determinations of REEs in the cores of the minerals, eliminating contributions from surface or rim enrichments in trace elements. Their study represents, to our knowledge, one of the few in situ studies that have successfully determined most of the LREE concentrations in olivine (Kennedy et al. (1993) also measured LREE partition coefficients in olivine but, because they did not measure clinopyroxene, their data are not shown). These in situ partition coefficients show no hint of parabolic dependencies with cationic radii, even for ol/cpx. The slope of the mineral/cpx versus cationic radii curves are similar to the slopes seen in our study and those of Stosch (1982) and Eggins et al. (1998) for the HREEs and MREEs. The slight offset between these experimental studies and studies based on peridotite xenoliths are likely due to a difference in temperature (as explained in the Section 4 below).

The progressive "straightening out" of the parabolas from leached bulk mineral dissolution studies to in situ studies, indicates that the positive correlation of apparent LREE ol/cpx and opx/cpx partition coefficients with cationic radii in bulk mineral dissolution studies is due to preferential surface enrichments of LREEs in olivine and

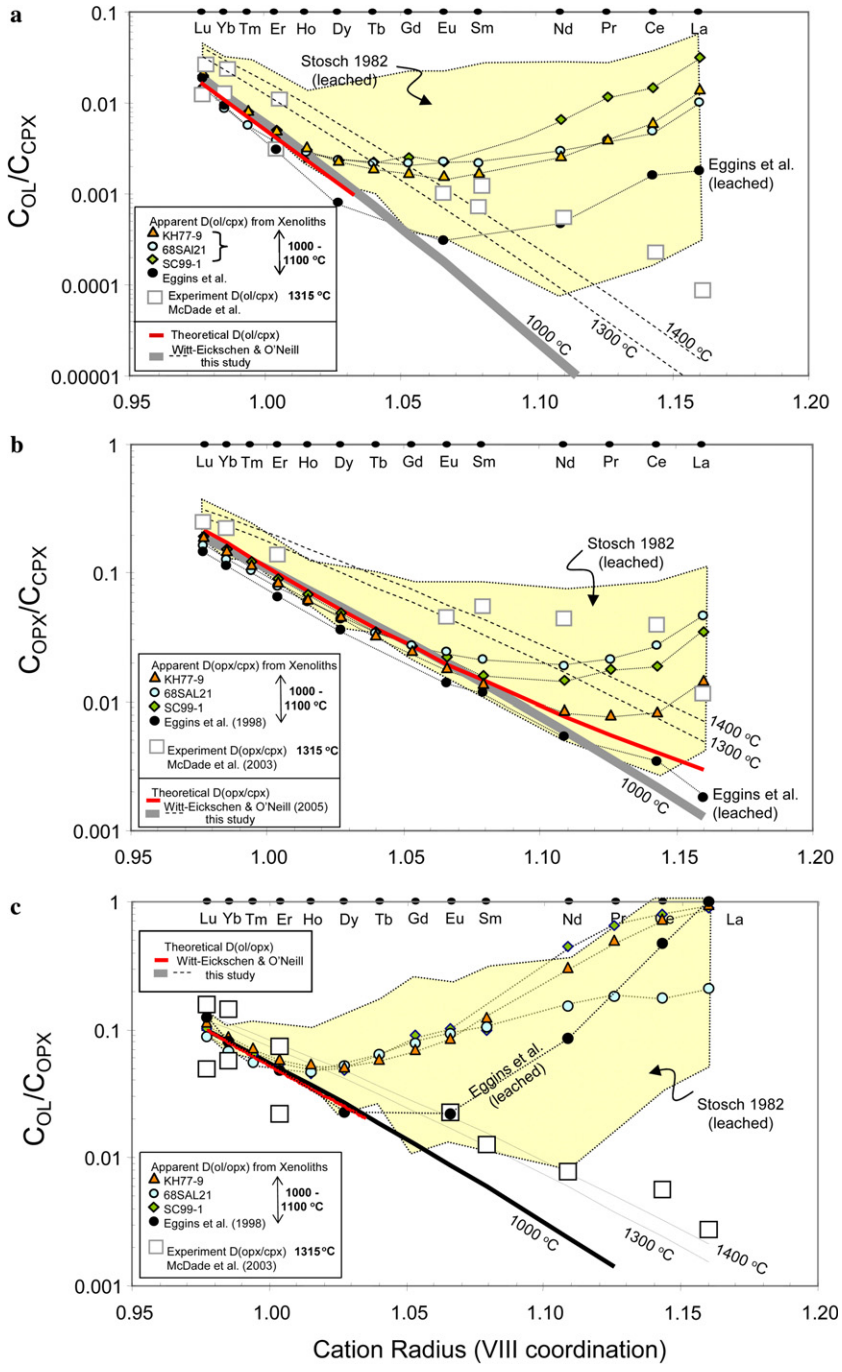

Fig. 2. Ol/Cpx (a), Opx/Cpx (b) and Ol/Opx (c) partition coefficients plotted versus cationic radii in 8-fold coordination. Colored symbols (blue circles, orange triangles, green diamonds) represent apparent subsolidus (1000–1100 °C) partition coefficients determined from unleached western USA xenoliths (this study). Black-circled line and yellow-shaded region correspond to partition coefficients determined on surface-leached minerals from spinel peridotite xenoliths (Stosch, 1982; Eggins et al., 1998). Experimental mineral/mineral partition coefficients from McDade et al. (2003) determined at solidus conditions (1300 °C, 1.5 GPa) are shown for reference (open squares). Thick gray line represents Ol/Cpx and Opx/Cpx partition coefficients at 1000 °C determined by fitting appropriate forms of Eq. (9) to the HREEs in (a) and HREEs and MREEs in (b). Dashed lines labeled 1300 and 1400 °C represent extrapolations of Eq. (9) to higher temperatures using fit parameters determined at 1000 °C from the apparent partition coefficients. Bold solid red line represents an empirical relationship between subsolidus partition coefficient and cationic radii from Witt-Eickschen and O'Neill (2005) corrected to 1000 °C. (For interpretation of the references to colors in this figure legend, the reader is referred to the web version of this paper.)

orthopyroxene compared to clinopyroxene. By contrast, the collapse of HREE and MREE partition coefficients in all studies to the same negatively correlated trend with cationic radius indicates that the HREEs and MREEs have not been affected significantly by metasomatic enrichments or other contaminating effects. Indeed, HREEs and MREEs have been shown to be less affected by metasomatic processes than LREEs as they are not typically as

enriched as the LREEs in metasomatic fluids/melts (Canil, 2004).

4. Discussion

Our first goal is to assess the applicability of lattice strain theory to subsolidus partitioning of REEs. Our second goal is to more quantitatively investigate the reasons for apparent LREE enrichment seen in bulk mineral dissolutions of olivine and orthopyroxene as discussed above. This will involve scrutiny of equilibrium and disequilibrium grain boundary enrichment phenomena. We will discuss how lattice strain theory can be used to "see through" the effects of LREE enrichment on grain boundaries, allowing us to improve estimates for LREE partition coefficients (e.g., unadulterated by LREE enrichment) by extrapolation of the model to large cationic radii.

4.1. Elastic strain theory and partition coefficients

We begin with mineral/melt partitioning where we approximate the exchange of a trace element (denoted by REE for instance) between clinopyroxene and melt as

$$\mathrm{REEAlSiO_6(cpx)} = \mathrm{REEAlSiO_6(melt)} \quad (1)$$

where REE substitution is coupled with Al for charge balance. For this reaction, the equilibrium constant is

$$K = a^{\mathrm{melt}}_{\mathrm{REEAlSiO_6}} / a^{\mathrm{cpx}}_{\mathrm{REEAlSiO_6}} \quad (2)$$

If the activity coefficients of the REE-pyroxene component in the melt and in cpx are similar and the molecular weight of the melt and cpx are similar, then Eq. (2) is roughly equivalent to the inverse of the Nernst-partition coefficient, $D^{\mathrm{cpx}}/^{\mathrm{melt}} \sim C^{\mathrm{cpx}}/C^{\mathrm{melt}}$, where C refers to the weight concentration of the trace element in the melt or clinopyroxene.

Blundy and Wood (1994) described the mineral/melt partitioning of a trace element i of given ionic radius r_i using the Brice formulation (Brice, 1975; Wood and Blundy, 1997):

$$D_i^{\mathrm{cpx/melt}} = D_{\mathrm{o}}^{\mathrm{cpx/melt}} \times \exp\left(\frac{-4\pi N_{\mathrm{A}} E_{\mathrm{cpx}}}{RT}\left[\frac{r_{\mathrm{o}}^{\mathrm{cpx}}}{2}(r_{\mathrm{o}}^{\mathrm{cpx}} - r_i)^2 - \frac{1}{3}(r_{\mathrm{o}}^{\mathrm{cpx}} - r_i)^3\right]\right) \quad (3)$$

This equation describes the partitioning of any given element i with respect to a reference element of given charge and which fits into a given lattice site of optimal radius r_{o} (all symbols and units are presented in Table 3). The partition coefficient of this optimum element is given by $D_{\mathrm{o}}^{\mathrm{cpx/melt}}$, which depends on temperature and pressure. The effective Young's modulus, E_{cpx} (GPa), is a measure of the stiffness of the bond between the cation and surrounding anions. It is a function of the charge of the substituting ion and the geometry of the site itself and as such, represents a site-specific effective Young's modulus, which does not in general equate exactly with any true Young's moduli of a crystal. In practice, $D_{\mathrm{o}}^{\mathrm{cpx/melt}}$ is not known *a priori* or may not even correspond to a real element, hence a more practical representation of Eq. (3) is to recast it in terms of a reference element, whose partition coefficient has been measured (Wood and Blundy, 2003). For example, Eq. (3) written in terms of a known Lu^{3+} partition coefficient is given by

Table 3
List of symbols

	Name	Value	Estimated (2STD) uncertainty	Units	Reference
Constants and Symbols					
Cpx	Clinopyroxene				
Opx	Orthopyroxene				
Ol	Olivine				
N_{A}	Avogadro's Number	6.02×10^{23}			
R	Gas constant	8.314		J/mol K	
T	Temperature			K	
r	Cation radius			Å	
r_{o}(cpx)	Optimum cpx cation radius	1.0		Å	Wood and Blundy (2003)
E_{cpx}	Effective cpx Young's modulus	318		GPa	Wood and Blundy (2003)
C	Concentration			ppm	
$D_{x/y}$	Partition coefficient between phases x and y				
$d_{\mathrm{gb/gm}}$	Grain boundary/matrix partition coefficient				
Fit parameters					
r_{o}(Opx)	Optimum opx cation radius	0.9	0.2	Å	
r_{o}(Ol)	Optimum ol cation radius	0.81	0.2	Å	
E_{Opx}	Effective opx Young's modulus	340	40	GPa	
E_{Ol}	Ol Young's modulus	370	40	GPa	

$$D_i^{\mathrm{cpx/melt}} = D_{\mathrm{Lu}}^{\mathrm{cpx/melt}} \times \exp\left(\frac{-4\pi N_{\mathrm{A}} E_{\mathrm{cpx}}}{RT}\left[\frac{r_{\mathrm{o}}^{\mathrm{cpx}}}{2}\left(r_{\mathrm{Lu}}^{\mathrm{cpx}^2} - r_i^2\right) - \frac{1}{3}\left(r_{\mathrm{Lu}}^{\mathrm{cpx}^3} - r_i^3\right)\right]\right) \quad (4)$$

Eq. (4) allows us to predict the partition coefficient of any other triply-charged element once the partition coefficient of our reference element Lu, $D_{\mathrm{Lu}}^{\mathrm{cpx/melt}}$, is used to pin the curve. The effects of temperature, pressure and major element composition are hidden in the $D_{\mathrm{Lu}}^{\mathrm{cpx/melt}}$ term, thus a value of $D_{\mathrm{Lu}}^{\mathrm{cpx/melt}}$ appropriate for the temperature, pressure and composition of interest must first be established (composition may also affect, to a lesser extent, the terms E and r_{o}, hence if the fit parameters to Eq. (4) are taken as constants, they should not be applied over too large a compositional range in clinopyroxenes).

The concept represented by Eq. (4) can be extended to partitioning between two mineral phases. For example, the exchange of REEs between clinopyroxene and olivine:

$$\mathrm{REEMgAlSiO_6(cpx)} + \mathrm{Mg_2SiO_4(ol)} = \mathrm{REEMgAlO_4(ol)} + \mathrm{Mg_2Si_2O_6(cpx)} \quad (5)$$

gives an equilibrium constant

$$K = \left(a_{\mathrm{REEMgAlO_4}}^{\mathrm{ol}} a_{\mathrm{En}}^{\mathrm{cpx}}\right)/\left(a_{\mathrm{REEMgAlSiO_6}}^{\mathrm{cpx}} a_{\mathrm{Fo}}^{\mathrm{ol}}\right) \quad (6)$$

where En (Mg_2SiO_4) and Fo (Mg_2SiO_4) refer to the enstatite component in pyroxene and the forsterite component in olivine. Again, assuming the forsterite and enstatite activity coefficients roughly cancel each other out their ratios are relatively constant within the compositional range of interest, the activities in Eq. (6) can approximately replaced by weight concentrations for practical purposes:

$$K \sim D^{\mathrm{ol/cpx}} = C_{\mathrm{REE}}^{\mathrm{ol}}/C_{\mathrm{REE}}^{\mathrm{cpx}} \quad (7)$$

To extend the Blundy and Wood (1994) model to mineral/mineral partitioning, we need only divide a cpx/melt partition coefficient (Eq. (4)) by a similarly formulated ol/melt partition coefficient:

$$D_i^{\mathrm{ol/melt}} = D_{\mathrm{Lu}}^{\mathrm{ol/melt}} \times \exp\left(\frac{-4\pi N_{\mathrm{A}} E_{\mathrm{ol}}}{RT}\left[\frac{r_{\mathrm{o}}^{\mathrm{ol}}}{2}\left(r_{\mathrm{Lu}}^{\mathrm{ol}^2} - r_i^2\right) - \frac{1}{3}\left(r_{\mathrm{Lu}}^{\mathrm{ol}^3} - r_i^3\right)\right]\right) \quad (8)$$

Dividing Eq. (8) by Eq. (4) yields the partitioning of an element i between cpx and ol at a given temperature (and pressure)

$$D_i^{\mathrm{ol/cpx}} = \frac{D_i^{\mathrm{ol/melt}}}{D_i^{\mathrm{cpx/melt}}} = D_{\mathrm{Lu}}^{\mathrm{ol/cpx}} \times \exp\left(\frac{-4\pi N_{\mathrm{A}}}{RT}\left[\frac{1}{2}\left(r_{\mathrm{Lu}}^2 - r_i^2\right)\left(E_{\mathrm{ol}} r_{\mathrm{o}}^{\mathrm{ol}} - E_{\mathrm{cpx}} r_{\mathrm{o}}^{\mathrm{cpx}}\right) + \frac{1}{3}\left(r_i^3 - r_{\mathrm{Lu}}^3\right)\left(E_{\mathrm{ol}} - E_{\mathrm{cpx}}\right)\right]\right) \quad (9)$$

As discussed in the Section 3, Eqs. (8) and (9) assume that the effective cationic radii in olivine and clinopyroxene are both in eightfold coordination number (r_{VIII}). Doing so greatly simplifies the mathematical representation of Eq. (9) (this can be verified by the reader). For olivine, a sixfold coordinated effective radii would have been more realistic, but treating the system in this way would result in several extra constants and a much more complicated formulation for Eq. (9). By assuming effective cationic radii based on the same cation coordination in olivines and pyroxenes, these extra constants are simply subsumed in the fit parameters of the present form of Eq. (9), giving us a more practical formulation to work with.

From Eq. (9), we can see that the dependency of $D_i^{\mathrm{ol/cpx}}$ on cationic radius is controlled by the effective Young's modulus (E) and optimum effective radius of the cation crystallographic site in each mineral (if they are identical, then there will be no dependency on cationic radius). In the case of mineral/melt partitioning, the difference between the cationic radius of the substituting element and the optimum site radius controls the misfit strain energy (see Eqs. (4) or (8)). Because the optimum site radius for olivine and orthopyroxene is smaller than that of clinopyroxene and because most of the REEs have cationic radii greater than r_{o} for clinopyroxene, this misfit strain energy is greatest for any given REE in olivine, intermediate in orthopyroxene, and smallest in clinopyroxene. Thus, Eq. (9) predicts that with increasing cationic radius, REEs should become more incompatible in olivine and orthopyroxene compared to clinopyroxene. Eq. (9) will be referred to from here on as a semi-empirical model to highlight that it is based on a functional form having physical significance (as opposed to an empirical parameterization with no explicit physical significance, e.g., in Witt-Eickschen and O'Neill (2005)).

We attempted to calibrate $D_i^{\mathrm{ol/cpx}}$ and $D_i^{\mathrm{opx/cpx}}$ as a function of cationic radius by fitting equivalent forms of Eq. (9) to the apparent $D_i^{\mathrm{ol/cpx}}$ and $D_i^{\mathrm{opx/cpx}}$ partition coefficients (Fig. 2). Before fitting, the following parameter values were adopted *a priori* (symbols and units given in Table 3): $r_{\mathrm{o}}^{\mathrm{cpx}}$ and E_{cpx} (Table 3) were adopted directly from a review paper by Wood and Blundy (2003), a temperature equivalent to that determined by two-pyroxene thermometry was assumed (1000 °C), and $D_{\mathrm{Lu}}^{\mathrm{ol/cpx}}$ (Table 2) was taken directly from the apparent partition coefficients measured in this study. The remaining parameters, $r_{\mathrm{o}}^{\mathrm{ol}}, r_{\mathrm{o}}^{\mathrm{opx}}$, E_{ol} and E_{opx} were determined by fitting the model to the observed data in Fig. 2 or Table 3. For $D_i^{\mathrm{ol/cpx}}$, we fit only to the HREEs. For $D_i^{\mathrm{opx/cpx}}$, we fit to the HREEs and MREEs. Values for $r_{\mathrm{o}}^{\mathrm{ol}}, r_{\mathrm{o}}^{\mathrm{opx}}$, E_{ol} and E_{opx} differ slightly from those of Wood and Blundy (2003) due to use of eightfold coordinated radii in this study. Uncertainties in the parameters at the 95% confidence level were estimated by randomly varying these parameters.

Several features are borne out by the application of lattice strain theory to mineral/mineral partitioning (Fig. 2). Fig. 2 shows that the semi-empirical values of $D_i^{\mathrm{ol/cpx}}$ and

$D_i^{opx/cpx}$ decrease roughly log-linearly with increasing r_i (readers who are familiar with the application of lattice strain theory to mineral/melt partitioning will note that, in mineral/melt partitioning, a concave downward parabola is typically seen when mineral/melt REE partition coefficients are plotted against cationic radii). The predicted monotonic decrease, however, is inconsistent with the apparent positive correlation between r_i and the apparent LREE $D_i^{ol/cpx}$ and $D_i^{opx/cpx}$ values. This deviation from theory for the LREEs is likely to be an artifact of trace-element enrichments on mineral grain boundaries as suggested in Section 3 and discussed later. The effects of surface contamination (or contamination by melt inclusions) should be most pronounced for the LREEs and for those elements with low REE concentrations in the host minerals (Zindler and Jagoutz, 1988). This is because melts are not only enriched in REEs, but are most enriched in LREEs due to the greater incompatibility of LREEs relative to HREEs during melting. LREE contamination should thus affect olivine the most, orthpyroxene second, and clinopyroxene last. This is consistent with the observation that apparent $D_i^{ol/cpx}$ deviate earlier from the trend predicted by the elastic strain model (in terms of r_i) than apparent $D_i^{opx/cpx}$. Clinopyroxene, in general should not be affected significantly by surface or inclusion contaminations.

Our explanation for the deviations of LREE partitioning from theory is further supported by considering the results of three independent studies. The first case concerns mineral partitioning studies of McDade et al. (2003) at solidus conditions. They report in situ measurements (ion microprobe) of all the REEs in olivine, clinopyroxene, and orthopyroxene in equilibrium with a basaltic melt, eliminating grain boundary effects. In a plot of $D_i^{min/cpx}$ versus r_i, a negative

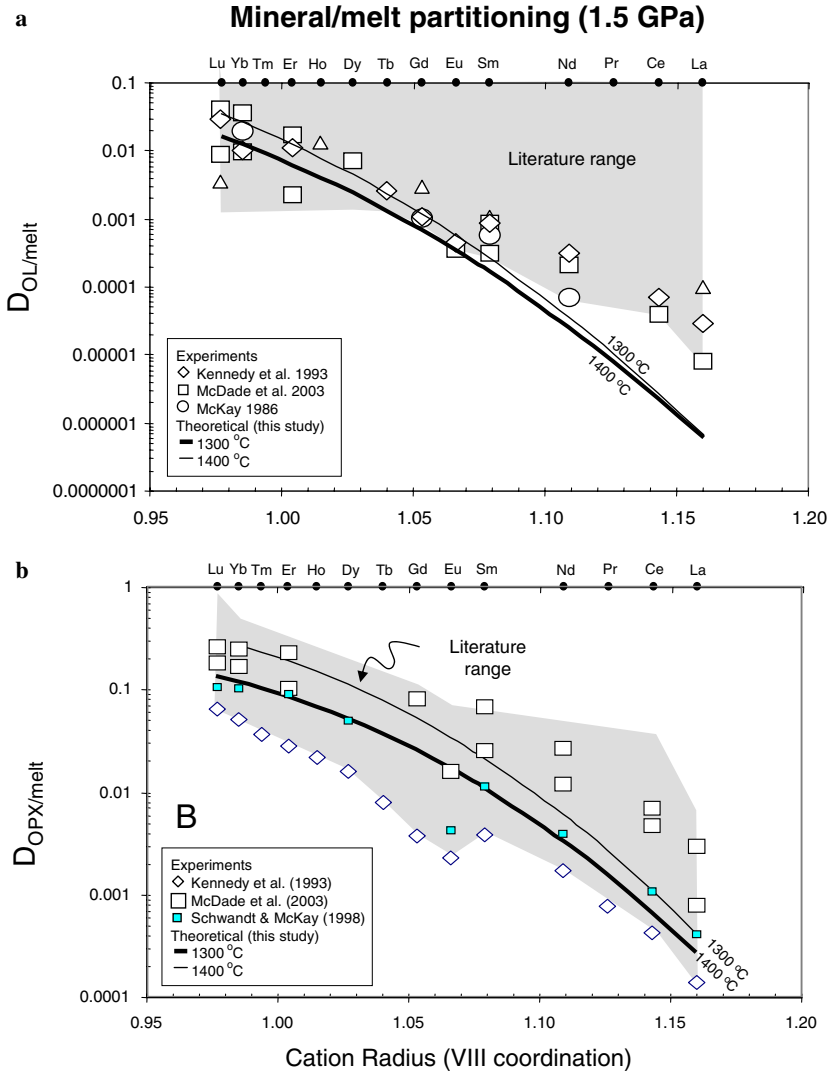

Fig. 3. Ol/Melt (a) and Opx/Melt (b) partition coefficients plotted against cationic radii. Curves represent theoretical values calculated at 1300 and 1400 °C by multiplying the appropriate calibrated forms of Eq. (9) by Cpx/Melt partition coefficients from Hauri et al. (1994) and McDade et al. (2003) for 1300 and 1400 °C, respectively; more details given in Table 4. Experimental values, which show the closest match to the calculated values, are shown for comparison. Gray shaded region represents literature range from Fig. 1.

correlation is seen, which is consistent with the semi-empirical trend predicted by Eq. (9). A similar consistency between our model and the McDade et al. data is seen in Ol/Opx partitioning (Fig. 3). The second case is represented by the combined studies of Stosch (1982) and Eggins et al. (1998), who measured apparent mineral/mineral element partitioning in various spinel lherzolites after subjecting their samples to acid-leaching (Fig. 2). The straightening out of the U-shaped curves in $D_i^{\mathrm{min/cpx}} - r_i$ space for leached samples indicates that high LREE contents of olivine and orthopyroxene relative to clinopyroxene are largely due to surface enrichments. The third case concerns the in situ study of peridotitic minerals by Witt-Eickschen and O'Neill (2005). They were able to develop purely empirical relationships between $D_i^{\mathrm{opx/cpx}}, D_i^{\mathrm{ol/cpx}}$ and r_i; their results, which should in theory be unaffected by grain boundary enrichments, are shown in Fig. 2 (thick bold red line). Their in situ measured partition coefficients coincide with our semi-empirical determined partition coefficients (note that they do not have LREE partition coefficients for olivine).

In summary, we demonstrate that HREE to MREE partitioning between the matrices of minerals in several independent studies are consistent with lattice strain theory. This lattice strain theory can thus be used to determine partition coefficients for the LREEs by extrapolation to suitable cationic radii.

4.2. Internally consistent REE partition coefficients for ultramafic minerals

The goal in this section is to estimate $D_i^{\mathrm{ol/melt}}$ and $D_i^{\mathrm{opx/melt}}$ for all REEs at the conditions of the peridotite solidus (within the spinel stability field). This requires correction of subsolidus values of $D_i^{\mathrm{ol/cpx}}$ and $D_i^{\mathrm{opx/cpx}}$ (1000–1100 °C) to temperatures relevant to melting conditions (1300 °C or higher at ~1.5 GPa). Once corrected for temperature, these values can then be multiplied by $D_i^{\mathrm{cpx/melt}}$ at the temperature of interest to obtain relevant $D_i^{\mathrm{ol/melt}}$ and $D_i^{\mathrm{opx/melt}}$. To correct for temperature, we first correct the pre-exponential factor in Eq. (9), $D_{\mathrm{Lu}}^{\mathrm{ol/cpx}}$ or $D_{\mathrm{Lu}}^{\mathrm{opx/cpx}}$, using the empirical temperature-dependency of Witt-Eickschen and O'Neill (2005) (note that while they have a global formulation for the effects of temperature for all REE partitioning, in the case of Opx/Cpx, they only have a formulation for the HREEs). For $D_{\mathrm{Lu}}^{\mathrm{opx/cpx}}$, the temperature correction we used was:

$$\ln D_{\mathrm{Lu}}^{\mathrm{cpx/opx}} = 18.11 - 0.192 r_{\mathrm{Lu}} + (-50568 + 542 r_{\mathrm{Lu}})/T + (-560755 + 10644 r_{\mathrm{Lu}} - 49.8 r_{\mathrm{Lu}}^2) N_{\mathrm{Na}}^{\mathrm{cpx}}/T \quad (10)$$

where r_{Lu} is in pm, T is in Kelvin, and $N_{\mathrm{Na}}^{\mathrm{cpx}}$ is the cation proportion of Na in clinopyroxene on a six oxygen basis taken here to be ~0.1 (see Table 1); note that Eq. (10) has been corrected from the original Eq. (5) in Witt-Eickschen and O'Neill for a typographical error (which we verified with O'Neill, personal communication). For $D_{\mathrm{Lu}}^{\mathrm{ol/cpx}}$, we used the following parametrization for temperature:

$$\ln D_{\mathrm{Lu}}^{\mathrm{cpx/ol}} = 0.19 + (3925 + 6600 N_{\mathrm{Na}}^{\mathrm{cpx}})/T \quad (11)$$

After pinning the curve to $D_{\mathrm{Lu}}^{\mathrm{ol/cpx}}$ and $D_{\mathrm{Lu}}^{\mathrm{opx/cpx}}$ at the temperature of interest, we then calculate the partition coefficients for the remaining REEs at this temperature using the lattice strain model presented in Eq. (9) (Table 4). To calculate mineral/melt partitioning, we then multiply these mineral/Cpx partition coefficients by known values of $D_i^{\mathrm{cpx/melt}}$. For 1300 °C, we use the data of McDade et al. (2003) at 1.5 GPa. For 1400 °C, we used the $D_i^{\mathrm{cpx/melt}}$ values at 1405 °C from Hauri et al. (1994). Unfortunately, not all of the REE partition coefficients were determined by these authors. We therefore estimated the partition coefficients of the missing elements by applying the elastic strain model (Eq. (3)) to Cpx/Melt partitioning using the experimentally determined $D_{\mathrm{Lu}}^{\mathrm{Cpx/Melt}}$ to pin the curve of $D_i^{\mathrm{Cpx/Melt}}$ versus r_i down (other parameters necessary for Eq. (3) are taken from Wood and Blundy (2003) and shown in Table 3). Table 4 and Fig. 3 show the recommended partition coefficients resulting from this study. Our semi-empirical estimates of $D_i^{\mathrm{ol/melt}}$ and $D_i^{\mathrm{opx/melt}}$ are otherwise independent in the sense that they are constrained from subsolidus partitioning and then extrapolated upwards in temperature.

It can be seen in Fig. 3a, that most literature $D_i^{\mathrm{ol/melt}}$ values are much higher than our calculated values. There is a closer match between our calculated $D_i^{\mathrm{opx/melt}}$ values and those determined from experiments and/or phenocryst-magma pairs. The discrepancy seen in Ol/Melt partition coefficients is most pronounced (up to several orders of magnitude) for apparent partition coefficients determined from phenocryst-magma pairs. In all likelihood, this discrepancy is due to lack of equilibrium and/or contamination of the phenocrysts by melt inclusions. The closest matches to our calculated $D_i^{\mathrm{ol/melt}}$ values are the experimental values from McKay (1986), Kennedy et al. (1993) and McDade et al. (2003). This consistency indicates that olivine strongly fractionates the REEs as previously suggested by McKay (1986). Experiments or phenocryst-magma studies that do not show this effect are probably incorrect. Nevertheless, we note that our calculated values are still slightly lower than the McKay, Kennedy et al., and McDade et al. experimental values of $D_i^{\mathrm{ol/melt}}$ for the LREEs. It is not clear if this small remnant discrepancy is real or an artifact of extrapolating our model to large cationic radii. Kennedy et al. cautioned that even in situ determined $D_i^{\mathrm{ol/melt}}$ for incompatible elements should be taken as maximum bounds owing to the possibility of micro-melt inclusions. These effects are more likely to be seen in olivine than in orthopyroxene because the former have very low levels of REEs and thus are easily overprinted by small amounts of contamination. We thus adopt our calculated mineral/melt partition coefficients for modeling melting processes in the next section. We caution, however, that partition coefficients are composition-dependent, so our recom-

Table 4
Recommended partition coefficients for basaltic systems (ppm/ppm)

	1200 °C		1300 °C					1400 °C						
	Ol/Cpx	Opx/Cpx	Ol/Cpx	Opx/Cpx	Cpx/Melt		Ol/Melt	Opx/Melt	Ol/Cpx	Opx/Cpx	Cpx/Melt		Ol/Melt	Opx/Melt
	This study	This study	This study	This study	McDade et al. (2003) 1315 °C	Interpolated 1315 °C	This study	This study	This study	This study	Hauri et al. (1994) 1405 °C	Interpolated 1405 °C	This study	This study
La	0.0000006	0.0013	0.000007	0.00486	0.08	0.086	0.000001	0.00042	0.000015	0.00711	0.051	0.038	0.000001	0.00027
Ce	0.0000017	0.0022	0.000018	0.00742	0.14	0.148	0.000003	0.0011	0.000035	0.0106	0.089	0.064	0.000002	0.00068
Pr	0.0000051	0.0036	0.000043	0.0112		0.239	0.000010	0.0027	0.000079	0.0156		0.10	0.000008	0.0016
Nd	0.000014	0.0059	0.00010	0.0168	0.317	0.361	0.000036	0.060	0.00017	0.0228	0.14	0.15	0.000026	0.0034
Sm	0.000084	0.0138	0.00041	0.0332	0.565	0.636	0.00026	0.021	0.00067	0.0433	0.3311	0.25	0.00017	0.011
Eu	0.00017	0.0197	0.00075	0.0443	0.367	0.766	0.00058	0.034	0.00117	0.0568	0.373	0.30	0.00035	0.017
Gd	0.00036	0.0279	0.00135	0.0587	0.990	0.891	0.0012	0.052	0.00202	0.0739		0.35	0.00070	0.026
Tb	0.00073	0.0393	0.00239	0.0773		1.00	0.0024	0.077	0.00347	0.0958		0.39	0.0013	0.037
Dy	0.00146	0.0548	0.00419	0.101		1.09	0.0046	0.11	0.00587	0.124	0.412	0.42	0.0024	0.052
Ho	0.00273	0.0742	0.00695	0.129		1.14	0.0079	0.15	0.00944	0.155		0.44	0.0041	0.068
Er	0.00479	0.0973	0.0110	0.161	1.10	1.16	0.013	0.19	0.0145	0.191	0.410	0.44	0.0064	0.085
Tm	0.00790	0.124	0.0164	0.196		1.16	0.019	0.23	0.0212	0.230		0.44	0.0094	0.10
Yb	0.0123	0.154	0.0235	0.0233	1.10	1.14	0.027	0.27	0.0298	0.271	0.413	0.44	0.013	0.12
Lu*	0.0182	0.186	0.0323	0.272	1.11	1.11	0.036	0.30	0.0400	0.313	0.425	0.43	0.017	0.13

"This study" = calculated using Eq. (9) using DLu (min/Cpx) as a known; temperature effect on Lu is determined using Witt-Eickschen and O'Neill (2005) "Cpx/Melt" partition coefficients from two studies are shown; "interpolated" column calculates D values for all REEs using lattice strain model of Wood and Blundy (2003) with DLu assumed "Ol/Melt" and "Opx/Melt" represent the partition coefficient resulting from multiplying mineral/Cpx partition coefficients by values in "interpolated" column.

mended values are considered most applicable to ultramafic systems within the spinel stability field.

4.3. Explanations for deviations of apparent LREE partitioning from theory

We now return to the observation that our apparent Ol/Cpx and Opx/Cpx subsolidus partition coefficients determined from the xenolith samples over-estimate theoretical predictions for the LREEs. In the above discussions, it was clear that these deviations are artifacts of enrichments in trace-elements on the mineral rims and that the effects would be most pronounced for the LREEs compared to the HREEs. We consider two possibilities here.

4.3.1. Disequilibrium effects: recent contamination of mineral surfaces by metasomatism

In this section, we consider the effects of contamination on grain boundaries by recent infiltration of the host lava or a metasomatic phase prior to eruption. This is the "standard" interpretation by the geochemical community (Zindler and Jagoutz, 1988). Assuming that the contaminating phase (recent metasomatism or contamination by host lava) on all minerals has the same composition, the bulk measured partition coefficient between two non-leached minerals, e.g., olivine and clinopyroxene, is given by

$$D^{\text{bulk}}_{\text{ol/cpx}} = \frac{C_{\text{ol}}X_{\text{ol}} + C_{\text{cont}}X_{\text{cont(ol)}}}{C_{\text{cpx}}X_{\text{cpx}} + C_{\text{cont}}X_{\text{cont(cpx)}}} \tag{12}$$

where X_{cont} refers to the weight fraction of the contaminating phase on olivine or clinopyroxene. For a contaminant having an upper continental crust-like trace element signature (Rudnick and Fountain, 1995), a ~0.1% level of contamination can explain the parabolic dependency of $D^{\text{bulk}}_{\text{ol/cpx}}$ and $D^{\text{bulk}}_{\text{opx/cpx}}$ versus cationic radius. Our choice of an upper continental crust trace-element composition as the contaminating phase is somewhat arbitrary. However, it is likely to be an approximate representation of the REE content and the LREE/HREE ratio of many hypothesized mantle metasomatic agents and some intraplate basalts. In any case, it can be seen that for a roughly spherical grain having a 1 mm radius (grain sizes in our xenoliths range from 1–2 mm in radius), the U-shaped data curves in Fig. 2 can be produced by a 0.3 micron layer of contaminant mantling the outer part of the mineral grains (see Fig. 4a). The take-home message is that simple contamination by a LREE-enriched metasomatic phase is a very plausible mechanism for explaining the deviations from theory seen in Fig. 2.

4.3.2. Equilibrium grain boundary partitioning: is it significant?

As an alternative, we also explore whether equilibrium grain boundary partitioning theory, recently extended from the material science community to the Earth science community (Hiraga et al., 2004), can also explain the deviations of our bulk-mineral dissolution-based observations from predictions based on elastic strain theory. In brief, Hiraga

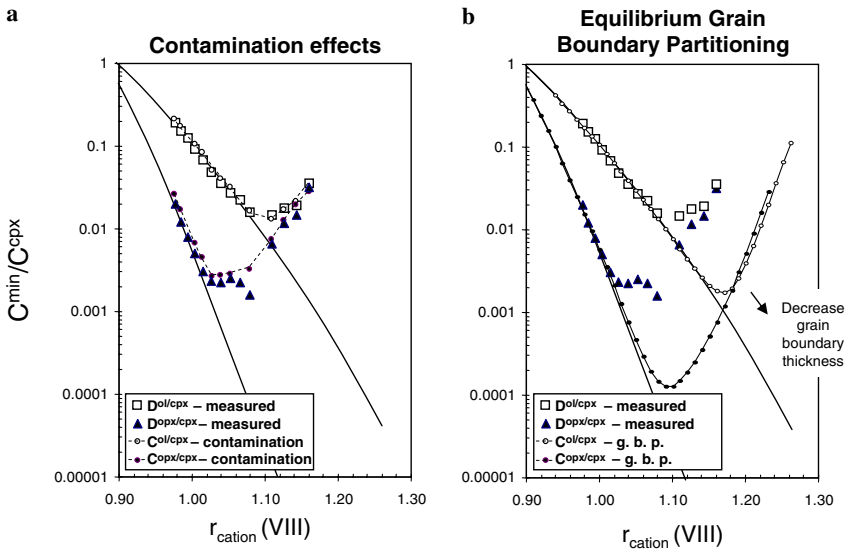

Fig. 4. Apparent subsolidus Ol/Cpx and Opx/Cpx partition coefficients plotted against cationic radii as in Fig. 2. Effects of rim enrichments in a LREE-enriched metasomatic component or contaminant are shown in (a). In this case, the metasomatic component was assumed to have a REE composition similar to that of upper continental crust (Rudnick and Fountain, 1995) although any other type of LREE-enriched contaminant could have been used and would have given the same result. Effects of equilibrium grain boundary enrichment (Hiraga et al., 2004) using the same elastic parameters for modeling partitioning in Fig. 2 are shown in (b). These calculations correspond to average grain radii of 0.5 mm and a grain boundary thickness of 10 nm, the latter of which represents the upper limit of grain boundary thicknesses. Decreasing grain boundary thicknesses causes the "U-shaped" patterns to deepen, which worsens the fit to the observed data (arrow points in direction of decreasing grain boundary thickness).

et al. suggest that grain boundaries (the few monolayers that make up grain boundaries and surfaces) are characterized by more expanded structures than grain interiors (matrices) due to the presence of more dislocations and point defects. As a consequence, under equilibrium conditions, a trace-element that is generally highly incompatible in a grain interior (matrix) could be preferentially segregated to the grain boundaries, resulting in an equilibrium enrichment of trace elements on the grain boundary (note that this is fundamentally different from contamination or recent metasomatism, which is a disequilibrium effect). Hiraga et al. suggest that grain boundaries could be significant repositories of highly incompatible trace elements in the upper mantle.

To explore this alternative, we adopt the model outlined in Hiraga et al. (2004). For dilute solutions, such as in the case of trace elements, the partitioning between the grain boundary (GB) and the grain interior or matrix (GM) is (McLean, 1957):

$$d_{\mathrm{GB/GM}} = \frac{C_{\mathrm{GB}}}{C_{\mathrm{GM}}} \sim \exp\left(\frac{U}{RT}\right) \tag{13}$$

where C is the weight concentration of an element, U is the energy associated with segregation of a trace element into the grain boundary, and a lower case d has been used to distinguish this "internal" partition coefficient from mineral-mineral matrix partitioning (note that grain matrix partitioning corresponds to what was discussed in Section 4.1). The segregation energy in a given mineral can be approximated by the misfit strain energy from matrix partitioning (identical to that used in Eq. (3); (Brice, 1975)):

$$U \sim 4\pi \mathrm{E} \mathrm{N_A}\left[\frac{r_{\mathrm{o}}}{2}(r_i - r_o)^2 + \frac{1}{3}(r_i - r_{\mathrm{o}})^3\right] \tag{14}$$

where the symbols are the same as in Eq. (3). It follows that the greater the difference between the radii of the substituting cation and the site radius $(r_i - r_{\mathrm{o}})$, the greater the segregation energy and grain boundary/matrix partition coefficient. This feature is shown in Fig. 4. Thus, the largest equilibrium grain boundary partition coefficients will be for olivine and the smallest will be for clinopyroxene. Recognizing that the measured bulk concentration of an element in a mineral, such as olivine, is given by $C_{\mathrm{ol}}^{\mathrm{bulk}} = C_{\mathrm{ol}}^{\mathrm{gm}} M_{\mathrm{ol}}^{\mathrm{gm}} + C_{\mathrm{ol}}^{\mathrm{gb}} M_{\mathrm{ol}}^{\mathrm{gb}}$, that is, the weighted average of the grain boundary and grain matrix, the theoretical bulk-determined partition coefficient $D_{\mathrm{bulk}}^{\mathrm{ol/cpx}}$ can be expressed in terms of the grain boundary/matrix partition coefficients $d_{\mathrm{gb/gm}}$ as

$$D_{\mathrm{bulk}}^{\mathrm{ol/cpx}} = \frac{C_{\mathrm{ol}}^{\mathrm{bulk}}}{C_{\mathrm{cpx}}^{\mathrm{bulk}}} = D_{\mathrm{gm}}^{\mathrm{ol/cpx}}\left[\frac{\left(d_{\mathrm{gb/gm}}^{\mathrm{ol}}\right)M_{\mathrm{ol}}^{\mathrm{gb}} + M_{\mathrm{ol}}^{\mathrm{gm}}}{\left(d_{\mathrm{gb/gm}}^{\mathrm{cpx}}\right)M_{\mathrm{cpx}}^{\mathrm{gb}} + M_{\mathrm{cpx}}^{\mathrm{gm}}}\right] \tag{15}$$

where M^{gb} and M^{gm} represent the mass fractions of the grain boundary and grain matrix relative to the bulk mineral grain; M^{gb} and M^{gm} can be estimated by assuming a fixed average grain size having a spherical geometry and uniform grain boundary thickness.

In Fig. 4b, we have attempted to fit Eq. (15) to the observed data by varying the grain boundary mass proportion, M_{gm} (which effectively corresponds to a grain

boundary thickness if the average grain diameter is defined). Assuming an average grain radius of 0.5 mm (we assume that the densities of the grain boundary and matrix are equal) and using the same effective Young's moduli and optimum site radii used in our treatment of matrix partitioning, we find that unreasonably large grain boundary thicknesses are required to match the "U-shaped" D versus r curves in Fig. 4b. In Fig. 4b, we show the case in which the grain boundary thickness is 10 nm. According to Hiraga et al., this is about the maximum thickness of an equilibrium grain boundary, which should be on the order of a few to ten monolayers. Decreasing the grain boundary thickness will result in a deeper trough on the D versus r plot, thus in order to exactly reproduce the apparent partition coefficient versus r curve, unreasonably large grain boundary thicknesses seem required. These observations suggest that equilibrium grain boundary partitioning is probably of lesser importance than contamination/metasomatism in explaining the enrichment in LREEs on olivine and orthopyroxene rims. A small effect from equilibrium grain boundary partitioning may still be present, but such an effect is not resolvable by our study, at least for the REEs. Our study does not rule out the possibility that equilibrium grain boundary partitioning is significant for other incompatible trace elements as suggested by Hiraga et al. More creative approaches will be needed to fully test the significance of equilibrium grain boundary partitioning.

4.4. Implications for bulk mineral dissolution studies and an approach for identifying trace element disequilibria

It is clear from this study that bulk mineral dissolution data should be interpreted cautiously if one is interested in determining trace element partitioning of olivines and orthopyroxenes. However, in the case of isotopic studies (such as Nd, Sr, and Hf isotopes), where bulk mineral dissolutions followed by chemical purification treatments are necessary, the theoretical framework provided here allows one to quantify the extent to which a mineral is in disequilibrium or is contaminated at its surface. Surface leaching of minerals should aid greatly in reducing the effects of surface contamination. However, the effects of infiltration of melts along microcracks or in the form of melt inclusions may be difficult to eliminate completely in olivine and even in orthopyroxene by leaching. To illustrate, for the olivine grains investigated in this study, 99.5% or more of the Nd is associated with grain boundary contamination (based on comparing apparent bulk measured concentrations to theoretical concentrations assuming that bulk Cpx concentrations are not affected significantly by grain boundary contamination—see Fig. 2). For the leached olivines of Eggins et al. (1998), 95% of the Nd is still of extraneous origin. Although orthopyroxene is less sensitive to grain boundary contamination than olivine, the effects can still be significant. In unleached samples, the contaminant represents up to 60% of the entire Nd budget of a bulk orthopyroxene grain.

Finally, even in the case of studies using in situ analytical techniques, the theoretical framework provided here can help in assessing whether minerals are in equilibrium. For example, our analysis can help to identify whether clinopyroxenes are in equilibrium with the bulk rock in a peridotite xenolith or abyssal peridotite. Some clinopyroxenes in highly depleted peridotites may have a metasomatic origin, but the question that arises is whether the metasomatic introduction was of ancient or recent introduction. Examining REE ratios between clinopyroxene, orthopyroxene and olivine (in situ or bulk dissolution) would hence be a useful approach in assessing disequilibria.

4.5. Implications of new olivine and orthopyroxene partition coefficients for harzburgite melting

Harzburgitic mantle rocks have been proposed as source materials for a variety of magmas, e.g., boninites (Falloon and Danyushevsky, 2000) and some hotspot magmas (Schaefer et al., 2002). In such cases, our new partition coefficients can be used to more precisely model trace-element systematics during magma genesis. We consider two cases here. Harzburgites (clinopyroxene-poor or -absent peridotites) occur in many REE flavors. Partially serpentinized ophiolitic peridotites, as exemplified by a case study (Fig. 5a) of the Feather River Ophiolite in California (Li and Lee, 2006), are LREE-depleted compared to the HREEs (see also Johnson et al. (1990) and Snow and Dick (1995)). In contrast, mantle xenoliths representing subcontinental lithospheric mantle are often LREE-enriched compared to the HREEs (Menzies, 1983; Hawkesworth et al., 1984; Richardson et al., 1984; Dawson, 1987; Menzies and Hawkesworth, 1987; Dawson and Smith, 1988; Griffin et al., 1988; Menzies, 1989; Hawkesworth et al., 1990; Griffin et al., 1999; Griffin et al., 2003; Pearson et al., 2003). Such LREE-enrichment often appears to be cryptic, that is, there are no significant changes in modal mineralogy or major element composition (Zindler and Jagoutz, 1988). An example of enriched subcontinental lithospheric mantle is shown in Fig. 5b for garnet-free harzburgite xenoliths from the Tanzanian craton (Rudnick et al., 1994; Lee and Rudnick, 1999; Lee, 2001). The exact origins of these LREE enrichments are unknown; there is probably no single process that gives rise to all LREE-enrichments. Some possibilities include chromatographic metasomatism imparted by porous melt flow (Navon and Stolper, 1987; Bodinier et al., 1990; Bedini et al., 1997) or infiltration and freezing in of small degree melts and fluids (Griffin et al., 1988; Zindler and Jagoutz, 1988; Rudnick et al., 1993; Ionov et al., 1995; Ionov et al., 1996; Li and Lee, 2006). A more detailed discussion on the origins of metasomatism, while interesting, is not the focus of this paper.

What do melts of these trace-element enriched lithologies look like? In Fig. 5c and d, we use the new Ol/melt and Opx/melt partition coefficients in Table 4 to calculate the REE abundance pattern of melts formed by 1% batch

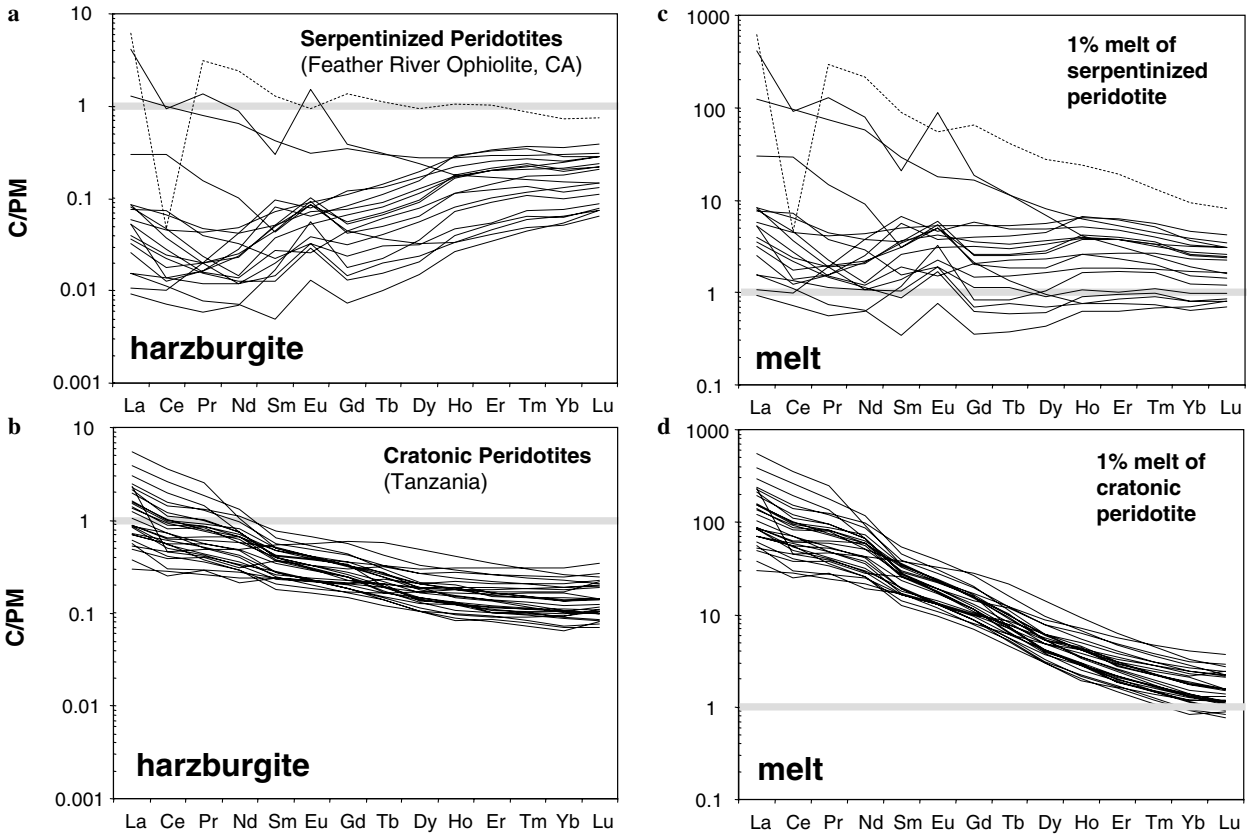

Fig. 5. REE abundance patterns of (a) serpentinized harzburgites from the Feather River ophiolite in northern California (Li and Lee, 2006) and (b) cryptically metasomatized spinel and chromite-bearing harzburgites from the Tanzanian craton (Lee, 2001). Composition of melts formed by 1% melting of such harzburgites are shown in (c) and (d). REE abundances normalized to primitive mantle composition (McDonough and Sun, 1995).

melting of the harzburgites in Fig. 5a and b. Because we are only looking for a rough estimate of abundance patterns, we assume for simplicity a constant (e.g., modal melting) modal mineralogy for all calculations (70% olivine, 30 orthopyroxene). We also assume that the REEs are hosted in and ultimately controlled by olivines and orthopyroxenes. It can be seen in Fig. 5 that small degree melting of trace-element depleted to enriched harzburgites can give rise to basaltic melts having flat REE abundance profiles to highly LREE-enriched abundance profiles. Melting of enriched harzburgites can even generate REE abundance patterns that resemble melts formed with garnet in the residue even if garnet is absent (Fig. 5d). Because melting of harzburgite (in the absence of volatiles) requires higher temperatures than that of fertile peridotite (lherzolite), it is likely that small degree re-melting of harzburgites occurs only locally, such as in plumes or during lithospheric extension.

5. Conclusions

This study presents a new set of olivine/melt and orthopyroxene/melt partition coefficients, which are internally consistent with clinopyroxene/melt partition coefficients, the latter of which are better constrained in the literature. Olivine and orthopyroxene strongly fractionate the rare-earth elements. We show that mineral/melt partitioning models based on lattice strain theory can be used to also explain mineral/mineral partitioning. This also provides a tool for testing whether REE contents in coexisting minerals are in equilibrium.

Acknowledgments

This research was supported by a fellowship from the Packard Foundation and the NSF (EAR 044003 and 0309121). Leeman acknowledges support from the NSF to continue his scientific research. Undergraduate Harbert was supported by the NSF and Rice University. Discussions with T. Hiraga, G. J. Wasserburg, H. St. O'Neill, A. Agranier, A. Lenardic, Z.-X. A. Li, M. Little, J. Blundy and Q.-Z. Yin are appreciated. We thank Wim van Westrenen, associate editor Fred Frey and an anonymous reviewer for providing critical and thoughtful reviews and for calling our attention to the important paper by Stosch (1982).

Associate editor: Frederick A. Frey

References

Bedini, R.M., Bodinier, J.-L., Dautria, J.M., Morten, L., 1997. Evolution of LILE-enriched small melt fractions in the lithospheric mantle: a case study from the East African Rift. *Earth Planet. Sci. Lett.* **153**, 67–83.

Blundy, J.D., Wood, B.J., 1994. Prediction of crystal-melt partition coefficients from elastic moduli. *Nature* **372**, 452–454.

Bodinier, J.L., Vasseur, G., Vernieres, J., Dupuy, C., Fabries, J., 1990. Mechanism of mantle metasomatism: geochemical evidence from the Lherz orogenic peridotite. *J. Petrol.* **31** (3), 597–628.

Brey, G.P., Kohler, T., 1990. Geothermobarometry in four-phase lherzolites II. New thermobarometers, and practical assessment of existing thermobarometers. *J. Petrol.* **31**, 1353–1378.

Brice, J.C., 1975. Some thermodynamic aspects of the growth of strained crystals. *J. Cryst. Growth* **28**, 249–253.

Canil, D., 2004. Mildly incompatible elements in peridotites and the origins of mantle lithosphere. *Lithos* **77**, 375–393.

Dawson, J.B., 1987. Metasomatized harzburgites in kimberlite and alkaline magmas; enriched restites and "flushed" lherzolites. In: Menzies, M.A., Hawkesowrth, C.J. (Eds.), *Mantle metasomatism*. Academic Press, pp. 125–144.

Dawson, J.B., Smith, J.V., 1988. Metasomatised and veined upper-mantle xenoliths from Pello Hill, Tanzania: evidence for anomalously-light mantle beneath the Tanzanian sector of the East African Rift Valley. *Contrib. Miner. Petrol.* **100**, 510–527.

Eggins, S.M., Rudnick, R.L., McDonough, W.F., 1998. The composition of peridotites and their minerals: a laser-ablation ICP-MS study. *Earth Planet. Sci. Lett.* **154**, 53–71.

Eggins, S.M., Woodhead, J.D., Kinsley, L., Mortimer, G.E., Sylvester, P., McCulloch, M.T., Hergt, J.M., Handler, M.R., 1997. A simple method for the precise determination of >40 trace elements in geological samples by ICP-MS using enriched isotope internal standardisation. *Chem. Geol.* **134**, 311–326.

Falloon, T.J., Danyushevsky, L.V., 2000. Melting of refractory mantle at 1.5, 2, and 2.5 GPa under anhydrous and H_2O-undersaturated conditions: implications for the petrogenesis of high-Ca boninites and the influence of subduction components on mantle melting. *J. Petrol.* **41**, 257–283.

Fujimaki, H., Tatsumoto, M., Aoki, K.-I., 1984. Partition coefficients of Hf, Zr, and REE between phenocrysts and groundmasses. *J. Geophys. Res.* **89**, 662–672.

Griffin, W.L., O'Reilly, S.Y., Abe, N., Aulbach, S., Davies, R.M., Pearson, N.J., Doyle, B.J., Kivi, K., 2003. The origin and evolution of Archean lithospheric mantle. *Precambrian Res.* **127**, 19–41.

Griffin, W.L., O'Reilly, S.Y., Ryan, C.G. (1999). The composition and origin of sub-continental lithospheric mantle. In: *Mantle Petrology: Field Observations and High Pressure Experimentation: A tribute to R. (Joe) Boyd*, vol. 6. Geochemical Society, pp. 13–45.

Griffin, W.L., O'Reilly, S.Y., Stabel, A., 1988. Mantle metasomatism beneath western Victoria, Australia: II. Isotopic geochemistry of Cr-diopside lherzolites and Al-augite pyroxenites. *Geochim. Cosmochim. Acta* **52**, 449–459.

Hart, S.R., Dunn, T., 1993. Experimental cpx/melt partitioning of 24 trace elements. *Contrib. Miner. Petrol.* **113** (1-8).

Hauri, E.H., Shimizu, N., Dieu, J.J., Hart, S.R., 1993. Evidence for hotspot-related carbonatite metasomatism in the oceanic upper mantle. *Nature* **365**, 221–227.

Hauri, E.H., Wagner, T.P., Grove, T.L., 1994. Experimental and natural partitioning of Th, U, Pb and other trace elements between garnet, clinopyroxene and basaltic melts. *Chem. Geol.* **117**, 149–166.

Hawkesworth, C.J., Kempton, P.D., Rogers, N.W., Ellam, R.M., van Calsteren, P.W., 1990. Continental mantle lithosphere, and shallow level enrichment processes in the Earth's mantle. *Earth Planet. Sci. Lett.* **96**, 256–268.

Hawkesworth, C.J., Rogers, N.W., Van Calsteren, P.W., Menzies, M., 1984. Mantle enrichment processes. *Nature* **311**, 331–335.

Hiraga, T., Anderson, I.M., Kohlstedt, D.L., 2004. Grain boundaries as reservoirs of incompatible elements in the Earth's mantle. *Nature* **427**, 699–703.

Ionov, D.A., O'Reilly, S.Y., Genshaft, Y.S., Kopylova, M.G., 1996. Carbonate-bearing mantle peridotite xenoliths from Spitsbergen: phase relationships, mineral compositions and trace-element residence. *Contrib. Mineral. Petrol.* **125**, 375–392.

Ionov, D.A., Prikhod'ko, V.S., O'Reilly, S.Y., 1995. Peridotite xenoliths in alkali basalts from the Sikhote-Alin, southeastern Siberia, Russia: trace-element signatures of mantle beneath a convergent continental margin. *Chem. Geol.* **120**, 275–294.

Irving, A.J., Frey, F.A., 1984. Trace-element abundances in megacrysts and their host basalts—constraints on partition-coefficients and megacryst genesis. *Geochim. Cosmochim. Acta* **48**, 1201–1221.

Johnson, K.T.M., Dick, H.J.B., Shimizu, N., 1990. Melting in the oceanic upper mantle: an ion microprobe study of diopsides in abyssal peridotites. *J. Geophys. Res.* **95**, 2661–2678.

Kennedy, A.K., Lofgren, G.E., Wasserburg, G.J., 1993. An experimental study of trace element partitioning between olivine, orthopyroxene, and melt in chondrules: equilibrium values and kinetic effects. *Earth Planet. Sci. Lett.* **115**, 177–195.

Larsen, L.M., 1979. Distribution of REE and other trace-elements between phenocrysts and peralkaline undersaturated magmas, exemplified by rocks from the Gardar Igneous province, South Greenland. *Lithos* **12**, 303–315.

Lee, C.-T. (2001). The origin, evolution, and demise of continental lithospheric mantle: perspectives from Re-Os isotopes, geochemistry, petrology, and modeling, Harvard University, Ph.D. thesis.

Lee, C.-T., Rudnick, R.L. (1999). Compositionally stratified cratonic lithosphere: petrology and geochemistry of peridotite xenoliths from the Labait Volcano, Tanzania. In: Gurney, J.J., Gurney, J.L., Pascoe, M.D., Richardson, S.R. (Eds.), *Proc. VIIth International Kimberlite Conference, B.J. Dawson volume*, pp. 503–521.

Lee, C.-T.A., 2003. Compositional variation of density and seismic velocities in natural peridotites at STP conditions: implications for seismic imaging of compositional heterogeneities in the upper mantle. *J. Geophys. Res.* **108**, 2441. doi:10.1029/2003JB002413.

Li, Z.-X.A., Lee, C.-T.A. (2006). Geochemical investigation of serpentinized oceanic lithospheric mantle in the Feather River Ophiolite, California: implications for the recycling rate of water by subduction. *Chem. Geol.* in press, doi:10.1016/j.chemgeo.2006.06.011.

Matsui, Y., Onuma, N., Nagasawa, H., Higuchi, H., Banno, S., 1977. Crystal structure control in trace element partition between crystal and magma. *Tectonics* **100**, 315–324.

McDade, P., Blundy, J.D., Wood, B.J., 2003. Trace element partitioning on the Tinaquillo lherzolite solidus at 1.5 GPa. *Phys. Earth Planet. Int.* **139**, 129–147.

McDonough, W.F., Sun, S.-S., 1995. The composition of the Earth. *Chem. Geol.* **120**, 223–253.

McKay, G.A., 1986. Crystal/liquid partitioning of REE in basaltic systems: extreme fractionation of REE in olivine. *Geochim. Cosmochim. Acta* **50**, 69–79.

McKay, G.A., Weill, D.F., 1977. KREEP petrogenesis revisited. *J. Geophys. Res.*, 2339–2355.

McKenzie, D., O'Nions, R.K., 1991. Partial melt distributions from inversion of rare Earth element concentrations. *J. Petrol.* **32**, 1021–1091.

McLean, D., 1957. *Grain boundaries in metals*. Clarendon, Oxford, 346 p.

Menzies, M., 1983. Mantle Ultramafic Xenoliths in Alkaline Magmas: Evidence for Mantle Heterogeneity Modified by Magmatic Activity. In: Hawkesworth, C.J., Norry, M.J. (Eds.), *Continental Basalts and Mantle Xenoliths*. Shiva Publishing Limited, p. 272.

Menzies, M.A., 1989. Cratonic, circumcratonic and oceanic mantle domains beneath the western United States. *J. Geophys. Res.* **94**, 7899–7915.

Menzies, M.A., Hawkesworth, C.J. (1987). Mantle metasomatism. In: *Academic Press Geology Series*, Academic Press Inc, p. 472.

Navon, O., Stolper, E., 1987. Geochemical consequences of melt percolation—the upper mantle as a chromatographic column. *J. Geol.* **95**, 285–307.

Nielsen, R.L., Gallahan, W.E., Newberger, F., 1992. Experimentally determined mineral-melt partition coefficients for Sc, Y and REE for olivine, orthopyroxene, pigeonite, magnetite and ilmenite. *Contrib. Mineral. Petrol.* **110**, 488–499.

Onuma, N., Higuchi, H., Wakita, H., Nagasawa, H., 1968. Trace element partition between two pyroxenes and the host lava. *Earth Planet. Sci. Lett.* **5**, 47–51.

Pearson, D.G., Canil, D., Shirey, S., 2003. Mantle samples included in volcanic rocks: xenoliths and diamonds. In: Holland, H.D., Turekian, K.K. (Eds.), *Treatise of Geochemistry*, vol. 2. Elsevier, pp. 171–275.

Richardson, S.H., Gurney, J.J., Erlank, A.J., Harris, J.W., 1984. Origin of diamonds in old enriched mantle. *Nature* **310**, 198–202.

Rudnick, R.L., Fountain, D.M., 1995. Nature and composition of the continental crust: a lower crustal perspective. *Rev. Geophys.* **33**, 267–309.

Rudnick, R.L., McDonough, W.F., Chappell, B.W., 1993. Carbonatite metasomatism in the northern Tanzanian mantle: petrographic and geochemical characteristics. *Earth Planet. Sci. Lett.* **114**, 463–475.

Rudnick, R.L., McDonough, W.F., Orpin, A., 1994. Northern Tanzanian peridotite xenoliths: a comparison with Kaapvaal peridotites and inferences of metasomatic reactions. In: Meyer, H.O.A., Leonardos, O.H. (Eds.), *Kimberlites, related rocks and mantle xenoliths*, vol. 1A. CPRM Special Publication, pp. 336–353.

Schaefer, B.F., Turner, S., Parkinson, I.J., Rogers, N.W., Hawkesworth, C.J., 2002. Evidence for recycled Archaean oceanic mantle lithosphere in the Azores plume. *Nature* **420**, 304–307.

Schnetzler, C.C., Philpotts, J.A., 1970. Partition coefficients of rare-earth elements between igneous matrix material and rock-forming mineral phenocrysts; II. *Geochim. Cosmochim. Acta* **34**, 331–340.

Schwandt, C.S., McKay, G.A., 1998. Rare earth element partition coefficients from enstatite/melt synthesis experiments. *Geochim. Cosmochim. Acta* **62**, 2845–2848.

Shannon, R.D., 1976. Revised effective ionic radii and systematic studies of interatomic distances in halides and chalcogenides. *Acta Crystallographica* **A32**, 751–767.

Shimizu, H., Sangen, K., Masuda, A., 1982. Experimental study on rare-earth element partitioning in olivine and clinopyroxene formed at 10 and 20 kb for basaltic systems. *Geochem. J.* **16**, 107–117.

Snow, J.E., Dick, H.J.B., 1995. Pervasive magnesium loss by marine weathering of peridotite. *Geochim. Cosmochim. Acta* **59**, 4219–4235.

Stosch, H.G., 1982. Rare earth element partitioning between minerals from spinel peridotite xenoliths. *Contrib. Mineral. Petrol.* **78**, 166–174.

Van Orman, J.A., Grove, T.L., Shimizu, N., 2001. Rare earth element diffusion in diopside: influence of temperature, pressure, and ionic radius, and an elastic model for diffusion in silicates. *Contrib. Mineral. Petrol.* **141**, 687–703.

Wells, P.R.A., 1977. Pyroxene thermometry in simple and complex systems. *Contrib. Mineral. Petrol.* **62**, 129–139.

Witt-Eickschen, G., O'Neill, H.S.C., 2005. The effect of temperature on the equilibrium distribution of trace elements between clinopyroxene, orthopyroxene, olivine and spinel in upper mantle peridotite. *Chem. Geol.* **221**, 65–101.

Wood, B.J., Blundy, J.D., 1997. A predictive model for rare earth element partitioning between clinopyroxene and anhydrous silicate melt. *Contrib. Mineral. Petrol.* **42**, 109–124.

Wood, B.J., Blundy, J.D., 2001. The effect of cation charge on crystal-melt partitioning of trace elements. *Earth Planet. Sci. Lett.* **188**, 59–71.

Wood, B.J., Blundy, J.D., 2003. Trace element partitioning under crustal and uppermost mantle conditions: the influences of ionic radius, cation charge, pressure, and temperature. *Treatise Geochem.* **2**, 395–424.

Zindler, A., Jagoutz, E., 1988. Mantle cryptology. *Geochim. Cosmochim. Acta* **52**, 319–333.